Effect of Harmonic Microstructure on the Corrosion Behavior of SUS304L Austenitic Stainless Steel

PRABHAT K. RAI, S. SHEKHAR, M. NAKATANI, M. OTA, S.K. VAJPAI, K. AMEYAMA, and K. MONDAL

Corrosion behavior of a harmonic structured SUS304L austenitic stainless steel was examined and compared with nonharmonic structured SUS304L stainless steel and conventional 304 stainless steel in 3.5 pct NaCl solution. The study was performed using linear polarization, potentiodynamic polarization, cyclic polarization, and a salt fog exposure test for 30 days. Characterization was accomplished using a scanning electron microscope, an electron probe microanalyzer, and Raman spectroscopy. Improved pitting corrosion resistance was found in the case of the harmonic structured steel as compared to that of the nonharmonic and the conventional 304 stainless steel. Harmonically distributed fine-grained structure, less porosity, and higher fraction of passive α-FeOOH are attributed to the improvement in corrosion resistance of the harmonic structured steel.

DOI: 10.1007/s11661-016-3758-2

I. INTRODUCTION

MATERIAL scientists and engineers are continuously involved in improving the properties of materials for better utilization. The contribution of the concept of the structure–property relationship has been proven to be vital in this quest. In this context, the classic work of Hall and Petch, famously known as the Hall–Petch relationship,[1] has played a pivotal role. This relationship suggests that the strength of material increases with the decrease in grain size. The past decades have witnessed high strength of nanocrystalline/ultrafine-grained (NC/UFG) materials developed *via* different processing routes such as high-energy ball milling,[2,3] severe plastic deformation of bulk material such as equal-channel angular pressing[4,5] and ultrasonic shot peening,[6,7] crystallization of amorphous precursors,[8] and electrodeposition.[9] These homogeneous NC/UFG materials suffer from a serious problem of extremely low ductility. In order to introduce ductility in the NC/UFG materials, bimodal structures have been introduced.[10–13] Plastic deformation of bimodal grain sized materials has been reported to be highly heterogeneous. Heterogeneity depends not only on the volume fraction of coarser grains but also on the grain size distribution.[14] Although an increase in ductility has been observed, it is extremely difficult to control the topology of grain size distribution by most of the available methods of preparing bimodal structure.[15] As a solution to the aforementioned problem with the NC/UFG materials, Ameyama and co-workers proposed the concept of "harmonic" structure design in materials, which has resulted in an ideal combination of high strength and ductility.[16–19] Harmonic structure is a bimodal structure with a specific topology of fine and coarse grains in a periodic or harmonic order. In this approach, high-energy ball milling is used under optimized parameters of ball-to-powder ratio, ball size, duration, and speed (rpm) of milling.[20,21]

Apart from mechanical properties, corrosion behavior of materials is highly dependent on grain refinement, as grain boundaries are highly reactive sites in the materials. The effect of grain size on the corrosion behavior has been studied extensively, but the results are still found to be contradictory. Both positive and negative impacts of grain refinement on corrosion resistance are reported.[22,23] Ralston *et al.*[24] studied the corrosion behavior of aluminum samples in 0.1 M NaCl solution with different grain sizes (~100 to ~2000 μm) developed by different processing routes and reported that a Hall–Petch type relationship may exist between grain size and corrosion rate. The reason for this behavior has been suggested to be the faster growth of protective oxides due to a decrease in grain size resulting in a decrease in corrosion rate. Zeiger *et al.*[25] studied the corrosion behavior of nanocrystalline FeAl8 alloy in Na_2SO_4 solution (pH 6) and found improved corrosion resistance of the nanocrystalline FeAl8 alloy due to faster diffusion of Al through grain boundaries, resulting in formation of protective passive film. Ye *et al.*[26] also reported the improved corrosion resistance

PRABHAT K. RAI, Ph.D. Student, S. SHEKHAR, Assistant Professor, and K. MONDAL, Associate Professor, are with the Department of Materials Science and Engineering, Indian Institute of Technology Kanpur, UP 208016, India. Contact e-mail: kallol@iitk.ac.in M. NAKATANI, Ph.D. Student, is with the Graduate School of Science and Engineering, Ritsumeikan University, Kusatsu, Shiga 5258577 Japan, M. OTA, Assistant Professor, and K. AMEYAMA, Professor, are with the Faculty of Science and Engineering, Ritsumeikan University, Kusatsu, Shiga 5258577, Japan. S.K. VAJPAI, Postdoctoral Fellow, is with the Research Organization of Science and Technology, Ritsumeikan University, Kusatsu, Shiga 5258577, Japan.

Manuscript submitted February 22, 2016.
Article published online October 20, 2016

of a nanocrystalline 309 stainless steel coating fabricated by DC magnetron sputtering in 0.5 M NaCl + 0.05 M H_2SO_4 solution due to the formation of compact and stable passive film on the coating. Gupta *et al.*[27] compared the corrosion behavior of the nanocrystalline and microcrystalline Fe20Cr alloy in 0.05 M H_2SO_4 and 0.05 M H_2SO_4 + 0.5 M NaCl solution and found improved passivating ability and pitting resistance due to the formation of passive film with higher Cr content.

In contrast to the preceding reports, some researchers have found adverse effects of grain refinement on the corrosion behavior of materials. Rofagha *et al.*[28] found the high corrosion rate of a nanocrystalline Ni (32-nm grain size) in 2 N H_2SO_4 solution compared to its coarse-grained counterparts (100-μm grain size) due to catalysis of the hydrogen reduction process by a large number of grain boundaries at the nanocrystalline surface. Oguzie *et al.*[29] also reported the increase in the corrosion rate of low carbon steel due to nanocrystalline coating on its surface. As discussed earlier, bimodal grain sized materials have found attention due to their better ductility over nanocrystalline counterparts. The corrosion behavior of bimodal grain sized materials has also been studied to some extent. However, detailed study is still warranted. Kus *et al.*[30] compared the corrosion behavior of nanocrystalline, coarse, and bimodal grained Al 5083 and found that the bimodal sample exhibits the lowest mass loss per unit area against nitric acid exposure, as bimodal samples are not susceptible to intergranular corrosion. Gollapudi[31] reported with the help of simulated data that the corrosion behavior of material having bimodal microstructure is improved with the increase in volume fraction of coarse grains in the nonpassivating medium and vice versa in the passivating medium. It is obvious that grain refinement does not always improve the corrosion resistance, and the same is true for conventional bimodal grain sized materials. Therefore, it is worth exploring the effect of uniformly distributed coarse and fine grains on the corrosion behavior of materials as a probable solution to the preceding problem.

Austenitic stainless steel is well known for its high corrosion resistance, and it is used in chemical processing equipment for dairy, food, and beverage industries and for bushings, shafts, valves, and heat exchangers.[32,33] Recently, harmonic structure design has been applied in a variety of materials, including stainless steel, and its effect on mechanical properties, such as strength, ductility, and hardness, has been studied.[33–35] Although the corrosion behavior of nanocrystalline materials has been studied extensively, as has that of bimodal grain sized materials to some extent, the corrosion behavior of harmonic structured materials has not been reported to date to the best of the authors' knowledge. Therefore, it is interesting to investigate the corrosion behavior of materials consisting of both ultrafine and coarse grains distributed in a harmonic order. Moreover, this would also indicate the significance of coarse and fine grains on the overall corrosion as well as electrochemical behavior if they are present in a harmonic fashion.

In the present work, an austenitic stainless steel (SUS 304L) was chosen for making sintered samples with nonharmonic and harmonic microstructures. These two samples with different microstructures developed *via* a sintering route from ball-milled powders were subjected to electrochemical tests [linear polarization (LP), dynamic polarization, and cyclic polarization] and a salt fog test in 3.5 pct NaCl solution. These samples were made at the laboratory of Professor K. Ameyama in Shiga, Japan. The electrochemical behavior of both the structures as well as their corrosion behavior have been compared and analyzed with the help of a scanning electron microscope (SEM), an electron probe microanalyzer (EPMA), and a Raman spectroscope. The corrosion products formed on the samples after a salt fog test for 30 days were analyzed to understand the corrosion behavior and mechanism of passivation in both structures. In addition, a conventional SUS304L plate of nearly similar composition was subjected to electrochemical tests to compare the effect of structures of the sintered harmonic and nonharmonic structured SUS304L with that of the conventional one.

II. MATERIAL AND METHODS

The initial powder of the SUS304L stainless steel was developed by the plasma rotating electrode process. The chemical composition of the SUS304L stainless steel powder is presented in Table I. It may be noticed that the carbon content is extremely low. The average particle size of the initial powder was measured to be ~120 μm. Mechanical milling was carried out under argon gas atmosphere at room temperature with the help of Fritch P-5 planetary ball mill using a steel vial and balls (diameter = 5 mm) made of SUS304 grade steel. The ball-powder mixture with a ball-to-powder weight ratio of 2:1 was milled for a duration of 180 ks at a constant milling speed of 200 rpm. Subsequently, the powders were sintered by spark plasma sintering (LABOX-675, NJS) at 1223 K (950 °C) for 3.6 ks (1 hour) under an applied pressure of 50 MPa and vacuum atmosphere. The sintering was carried out using a graphite die (internal diameter = 50.4 mm) and punch (outer diameter = 50 mm). The spark plasma sintering resulted in compacts with dimensions of 50-mm diameter × 17-mm thickness. A conventional SUS304L steel plate of near similar composition (Table I) was used for comparison of the corrosion behavior of the sintered harmonic and nonharmonic structured SUS304L steels. The conventional steel was heated to 1323 K (1050 °C) for an hour and water quenched.

For microstructural observations, specimens of three steels were initially ground successively with 240- to 1000-grit SiC papers followed by cloth polishing using alumina paste of 1-μm particle size. The specimens were cleaned ultrasonically with iso-propyl alcohol and were etched with 85 mL HCl and 15 mL HNO_3. Microstructures were examined with the help of a FEI Nova 450 finite-element SEM operating at 20 kV. Grain size calculations were done stereologically using the linear intercept method by determining the mean intercept length with the help of ImageJ software. The measurement of the volume fraction of fine and coarse grains as

Table I. Chemical Composition of Harmonic and Conventional SUS 304L Stainless Steels. Non-harmonic SUS 304L Has the Same Composition as the Harmonic Steel

Steel	C	Si	Mn	P	S	Ni	Cr	Fe
Harmonic	0.05	0.28	1.37	0.032	0.025	8.2	18.6	bal.
Conventional	0.054	0.45	1.64	0.037	0.43	8.1	17.6	bal.

well as porosity was carried out stereologically using the point counting method by applying a grid on the micrograph with the help of ImageJ software. The density measurement was done using the kit of Mettler Toledo XS 205 digital balance according to Archimedes' principle.

Specimens for electrochemical tests were cut in dimensions 4 mm × 8 mm × 1 mm using an EDM wire cutter followed by mechanical grinding to a surface finish of 600-grit SiC paper. After grinding, specimens were cleaned ultrasonically in iso-propyl alcohol. Electrochemical tests were carried out using a Parstat 2263 (Princeton Applied Research) potentiostat in a conventional round bottom cell. A saturated calomel electrode ($E_{SCE}^{o} = +241\ mV_{SCE}$) was used as a reference electrode, and platinum wire was used as a counter electrode. The tests were performed in a freely aerated 3.5 wt pct NaCl solution at ambient temperature. After 3600 seconds of stabilization, the value of the open circuit potential was obtained. Thereafter, LP, dynamic polarization, and cyclic polarization tests were carried out at a scan rate of 0.166 mV/s. After electrochemical tests, specimens were examined with the help of an SEM. Composition analysis of the specimens after dynamic polarization tests was carried out using a JEOL JXA-8230 EPMA. In order to understand the pitting behavior of the three different steels taken in this study, cyclic polarization tests were performed in 3.5 pct NaCl solution.

Specimens identical to those used in electrochemical tests were used for salt fog tests. According to ASTM-B 117,[36] specimens were hanged at 30 deg to vertical in the salt fog chamber after protecting the thickness region with the help of standard lacquer and Teflon tape. A 3.5 wt pct NaCl solution was used for maintaining fog in the chamber. The specimens were exposed to 3 hours of fog followed by 9 hours of drying for 30 days. Corrosion products formed on the specimens were characterized with the help of an FEI Nova 450 SEM and Acton SpectraPro SP-2500 Raman spectrometer using an excitation laser of 532-nm wavelength coupled with Olympus optical microscope.

III. RESULTS AND DISCUSSION

The SEM micrographs of the harmonic structured SUS304L austenitic stainless steel are shown in Figures 1(a) (low magnification) and (b) (high magnification). It can be noticed from Figures 1(a) and (b) that there is a heterogeneous microstructure (from grain size ranges) consisting of regular bimodal grain size distribution in the case of the harmonic structured steel. It is evident that islands of coarser grains (core) are surrounded by an interconnected network of ultrafine grains (shell). This trend is very regular all throughout the microstructure. The grain sizes are found to be ~23 μm in the core region and ~2 μm in the shell region. The volume fractions of the shell and core regions are measured to be ~26 and ~74 pct, respectively. This microstructure is similar to those reported in the different harmonic structured materials by the Ameyama's group.[33,34] Figures 1(c) (low magnification) and (d) (high magnification) show the SEM micrographs of the nonharmonic structured SUS304L stainless steel. Uniformly distributed equiaxed grains of average grain size ~28 μm can be observed in the micrograph of the nonharmonic structured steel. A significant amount of porosity can be observed in the micrograph of the nonharmonic structured steel, as shown in Figures 1(c) and (d), whereas no significant porosity can be found in the harmonic structured steel, as shown in Figures 1(a) and (b). A similar observation of significantly reduced porosity was reported by Sawangrat *et al.*[16] in the harmonic structured Co-Cr-Mo alloy and Zhang *et al.*[33] in the harmonic structured SUS304L steel. The approximate porosity was determined to be ~0.6 and ~2.2 pct in the case of the harmonic and nonharmonic structured steels, respectively. These pores can be formed due to improper consolidation of powder particles during sintering, which resulted in the formation of small cavities of size ~6 μm at the interparticle interfaces in the case of the nonharmonic steel (Figure 1(d)). The area fraction of pores was measured stereologically and found to be ~3.3 pct. The densities of the harmonic and nonharmonic structured SUS304L steels were measured to be ~7.85 and ~7.72 g/cm^3, respectively. This difference in the values of densities is attributed to the larger nonuniformly distributed pores in the case of the nonharmonic steel sample.

Figures 2(a) and (b) show the grain size distribution of the nonharmonic and the harmonic structured SUS304L steels, respectively. A large variation in grain size can be noticed in the case of the harmonic structured steel due to the presence of finer grains in the shell region as compared to the nonharmonic one. The grain boundary area fractions were ~4.1 and ~2.4 pct for the shell and core regions, respectively, in case of the harmonic structured steel. Moreover, 4.1 pct is calculated on the basis of the average fine grain boundary area fraction per unit of shell region of the harmonic structure. It should be mentioned that the 26 pct volume fraction of fine shell regions is distributed uniformly throughout the matrix. Apart from the fine grain fraction, the uniform distribution of the fine shell region is an equally important aspect, which would finally affect the corrosion and electrochemical behavior of these steels. In addition, even if the average grain

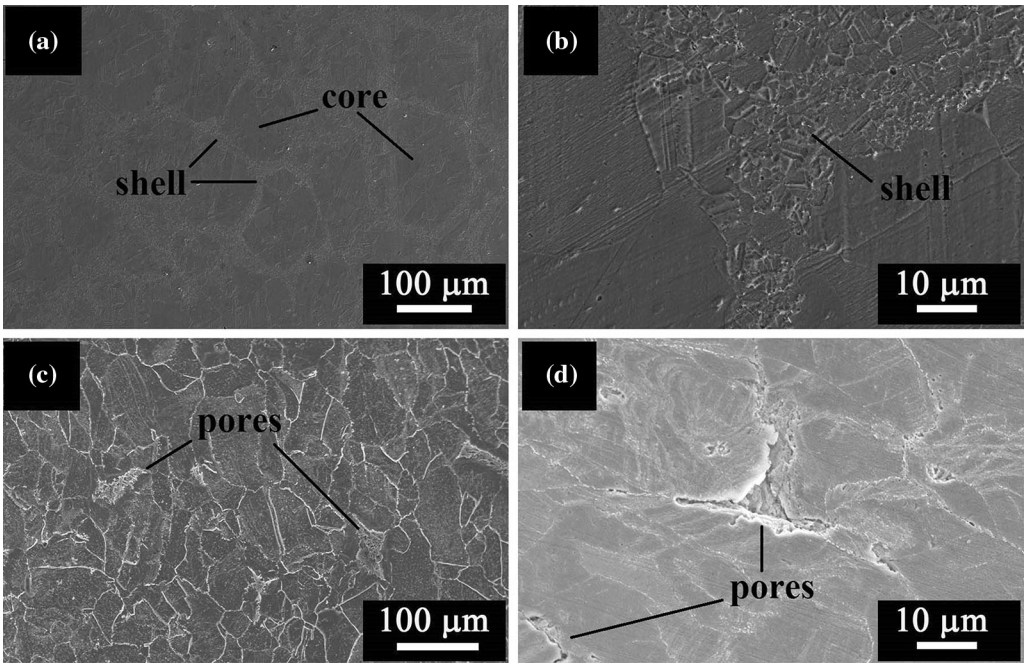

Fig. 1—SEM micrographs of (*a*) and (*b*) harmonic structured and (*c*) and (*d*) nonharmonic structured stainless steel showing different grain size distributions and pores.

boundary area is considered for the harmonic structured steel, it comes out to be ~2.8 pct. Hence, from the 2.1 pct grain boundary area fraction of the nonharmonic structured steel, the grain boundary area fraction has gone up by ~33 pct in the harmonic structured steel. This is a considerable increase, sufficient to influence the electrochemical behavior of the steels.

Figure 3(a) shows the SEM micrograph of the conventional SUS 304L steel plate. Figure 3(b) shows the grain size distribution in the same steel sample. Equiaxed grains of average grain size ~36 μm can be observed in the microstructure of the conventional SUS304L steel (Figure 3(a)). The grain size distribution in case of the conventional SUS304L stainless steel is shown in Figure 3(b). The grain boundary area fractions were found to be ~2.1 and ~1.7 pct in the case of the nonharmonic structured and conventional SUS304L steel, respectively.

The LP plots of the harmonic structure in the 3.5 pct NaCl solution, the conventional, and the nonharmonic structured stainless steels are shown in Figure 4(a). The polarization resistance (R_p) can be obtained from the slope of the LP plot given by Eq. [1] according to ASTM standard G102-89.[37]

$$\text{Polarization resistance}\left(R_p\right) = \left(\Delta E/\Delta i\right) \qquad [1]$$

The values of R_p were measured to be 181,081, 15,175, and 7142 Ohms cm^2 for the harmonic, the conventional, and the nonharmonic structured stainless steels, respectively. It can be observed from the values of R_p and Figure 4(a) that the slope for the harmonic structured steel (polarization resistance) is noticeably higher than that for the nonharmonic structured steel. It could be possible that the presence of a much finer grain size around the coarser grains in a systematic manner leads to uniform distribution of the active grain boundary zones. Moreover, there could be a distinct effect from a much larger fraction of the grain boundary area in the case of the harmonic structured steel, leading to a higher corrosion resistance as compared to the nonharmonic structured steel. Though the grain size of the conventional steel is larger than that of the harmonic coarse grain regions, it does not have any porosity. This would lead to higher polarization resistance as compared to the nonharmonic steel. On the other hand, higher polarization resistance of the harmonic steel, even as compared to the conventional steel, is attributed to the harmonic distribution of fine and coarse grains.

In order to investigate the response of material in a greater range of potential, dynamic polarization tests were carried out in the same solution of 3.5 pct NaCl, and the resulting plots are shown in Figure 4(b). The values of the corrosion current density (i_{corr}) were determined using Tafel extrapolation, and the corrosion rate (mm/year) was calculated from i_{corr}, according to ASTM standard G102-89.[37] The values of i_{corr} and corrosion rate (mm/year), as well other polarization parameters, for all three steels are presented in Table II. The dynamic polarization curves reveal lesser corrosion current density (i_{corr}) in the case of the harmonic structured steel as compared to that of the nonharmonic structured and the conventional SUS304L steels. Although these steels are of almost the same composition, they exhibit different corrosion rates. Moreover, the corrosion rate of the conventional steel lies in-between the harmonic and nonharmonic steels in line with the fact that polarization resistance of the conventional steel also lies in-between. Similarly, the corrosion potential (E_{corr}) of the conventional steel also lies

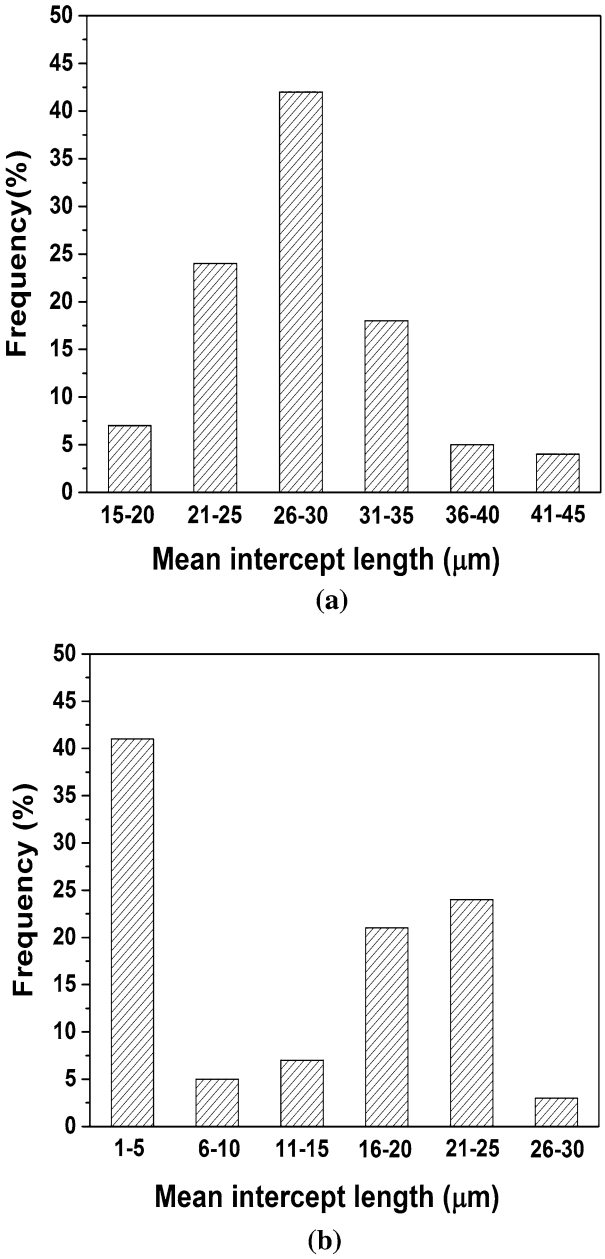

Fig. 2—Average grain size distribution of (*a*) nonharmonic and (*b*) harmonic structured stainless steel.

in-between (Table I). The reason for such observation is the same as provided while explaining the variation of the polarization resistance of three steels as obtained from LP.

Serrations and current fluctuations could be observed in the anodic branch of the polarization curve of the harmonic structured steel. These fluctuations indicate unstable passivation, whereas in the case of the nonharmonic structured steel, the passivation is quite stable with a much lesser serrated section in the passive zone. Two entirely different grain size distributions are present throughout the harmonic structured steel, which could lead to different rates of formation and breakage of passive film in the shell and core region. Since finer grains have higher grain boundary areas, the corrosion is localized in the finer-grained regions, leaving the coarse-grained section to reach stable passivation. This is a plausible explanation, since in the case of the nonharmonic steel, stable passivation is observed. Now, because of the closely spaced grain boundaries and much larger grain boundary area in the shell region, corrosion does not show preference to any sites in the case of the shell region of the harmonic structured steel, even though the corrosion is localized in the finer-grained region. Therefore, the corrosion attack is uniform in the fine-grained sections. Due to continuous formation and the breakdown of the passive layer along the finer grain boundary regions, the polarization plot also shows serration in the case of the harmonic structured steel. The preceding understanding is strongly supported by the completely smooth anodic regions of the conventional steel, where the grain size is larger and there is no porosity.

The SEM micrographs of the corroded specimens of the harmonic, nonharmonic, and conventional stainless steels, tested up to the same potential (in dynamic polarization tests under identical conditions), are shown in Figures 5(a), (b) and (c), respectively. The micrographs detect the morphology of the corroded surface. It is evident from the micrographs that the exposed surface of the harmonic structured SUS304L steel is less damaged compared to that of the nonharmonic structured and the conventional stainless steel. In order to investigate the depth of corrosion damage, the transverse face of the specimen perpendicular to the surface exposed to 3.5 pct NaCl was examined with the help of an SEM, and these micrographs are shown in Figures 6(a) through (c). A greater number of cracks and deeper damage in the case of the nonharmonic structured steel can be clearly noticed as compared to the harmonic structured and the conventional steel samples. This observation is in good agreement with the higher polarization resistance and lower corrosion current density obtained from electrochemical tests in the 3.5 pct NaCl solution in the case of the harmonic structured steel as compared to the nonharmonic structured steel. The conventional steel shows somewhat higher cracks and damage as compared to the harmonic structured steel (Figures 6(a) and (c)). However, it has much better protective cover than that of the nonharmonic structured steel (Figures 6(b) and (c)), which is also reflected in its lower corrosion current density.

The corroded surface of the harmonic structured steel was examined with the help of an SEM, as shown in Figures 7(a) and (b), after carrying out a dynamic polarization test up to a potential of 1 V. It can be noticed that relatively heavy material degradation took place along particular patterns, leaving the enclosed region less corroded. The diameter of the core region was found to be in the range of 130 to 150 μm, whereas the width of the shell region was found to be in the range of 15 to 25 μm in the microstructure of the noncorroded harmonic structured steel, as shown in Figure 1(a). Interestingly, the widths of heavily corroded and less corroded regions in Figure 7 are found to be in the same range as those of the shell and core regions in the

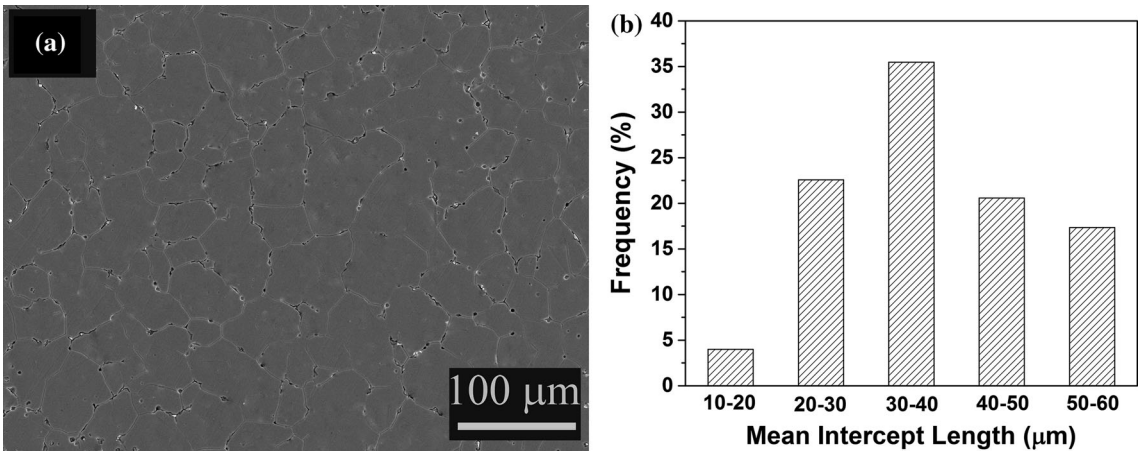

Fig. 3—(*a*) SEM micrograph and (*b*) average grain size distribution of the conventional 304 stainless steel.

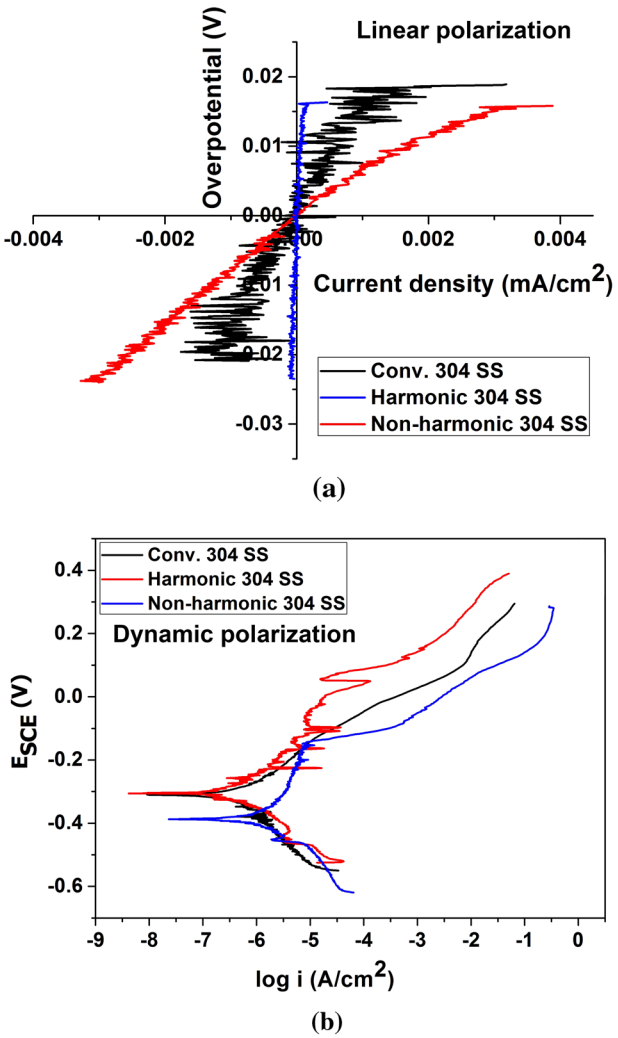

Fig. 4—(*a*) LP and (*b*) dynamic polarization plots of the harmonic, the nonharmonic, and the conventional stainless steel in 3.5 pct NaCl solution.

microstructure shown in Figure 1(a). The volume fractions of the heavily corroded and less corroded regions are determined stereologically by the point counting method and found to be ~31 and ~69 pct, respectively. These values are also comparable to the volume fractions of the shell and core regions in the noncorroded condition, as shown in Figures 1(a) and (b). Therefore, it can be concluded that corrosion is mainly limited to the shell region consisting of finer grains and that little corrosion takes place in the coarse-grained region.

In order to investigate the cause of differential corrosion in the shell and core regions, compositional analysis of the harmonic structured SUS304L was carried out using EPMA along a line originating from the middle of the core and passing through the shell region, as shown in Figure 8(a). It is evident from Figure 8(b) that the composition remains almost constant in the shell and core regions. Therefore, it can be concluded that heavy corrosion of the shell region is not due to chemical change. It is worth mentioning that the composition of the nonharmonic structured and conventional steels also remains uniform throughout, as determined from the EPMA study (data not shown). The higher rate of corrosion in the shell region can be attributed to the reduction in grain size resulting in an increase in fast diffusion channels, such as grain boundaries, for ions. The probable cause for reduction in the corrosion resistance of the nonharmonic structured SUS304L steel could be the pre-existing pores in the material. These pores may accelerate the process of corrosion. Although shell regions have corroded more in the harmonic structured steel, the net corrosion rate has been measured to be more in the nonharmonic one due to pre-existing porosity, as observed in Figures 1(c) and (d). However, there are no visible pores in the case of the harmonic structured steel (Figures 1(a) and (b)). The conventional 304 stainless steel has exhibited markedly higher corrosion resistance as compared to the nonharmonic stainless steel since it has no pores.

It is also important to observe that the core regions have the appearance of pop up, as compared to the shell regions, which form a trough in the case of the harmonic structured steel (Figure 7(b)). This also agrees with the plausible mechanism as proposed earlier while explaining the serration in the passive portion of the dynamic

Table II. Values of Electrochemical Parameters Obtained from Electrochemical Polarization in 3.5% NaCl Solution

Material	R_p (Ohms-cm^2)	β_a (mV/decade)	β_c (mV/decade)	E_{corr} (mV *vs* SCE)	i_{corr} (μA/cm^2)	Corrosion rate (mm/year)
Harmonic 304 SS	181,081	163	154	−308	0.47	0.0048
Non-harmonic 304 SS	7142	203	74	−387	0.93	0.0095
Conventional 304 SS	15,175	186	171	−310	0.56	0.0060

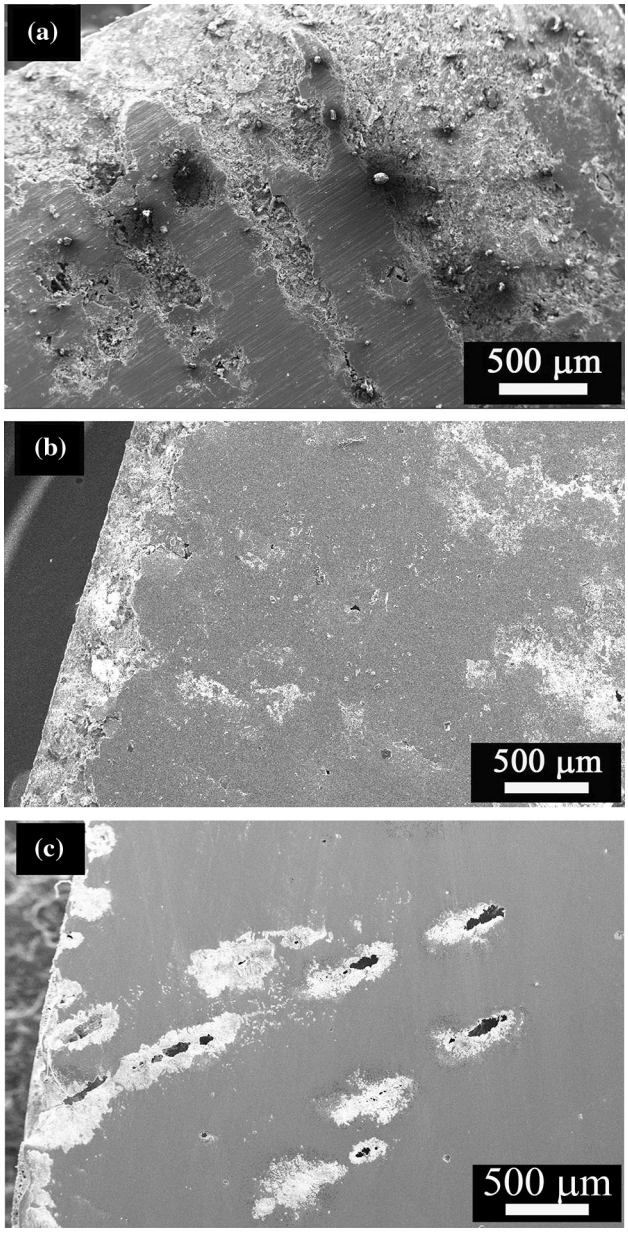

Fig. 5—SEM micrographs after dynamic polarization test in 3.5 pct NaCl solution for (*a*) the nonharmonic, (*b*) the harmonic, and (*c*) the conventional stainless steels.

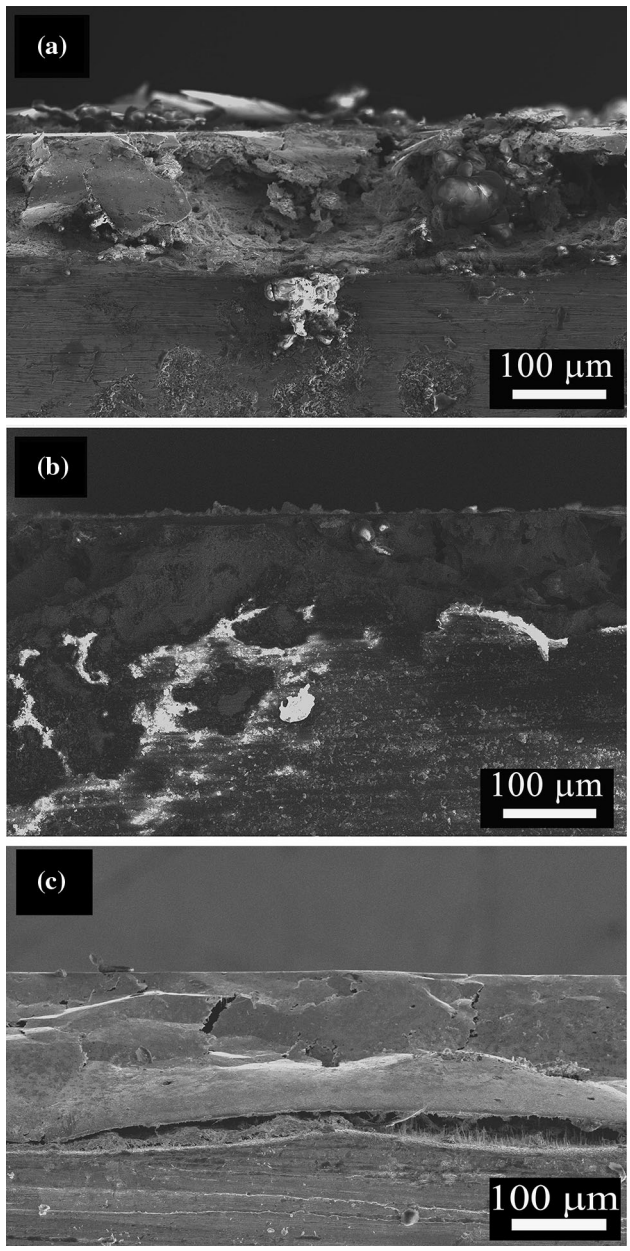

Fig. 6—SEM micrographs showing the cross-sectional surface of specimens in a dynamic polarization test in 3.5 pct NaCl solution for (*a*) the nonharmonic, (*b*) the harmonic, and (*c*) the conventional stainless steels.

polarization plot (Figure 4(b)). Since the passivation is unstable in the shell (fine-grained) regions, the dissolution would be greater in the fine-grained region as compared to the coarse-grained core region, leading to the pop up (coarse-grained sites) and trough (fine-grained sites) zones.

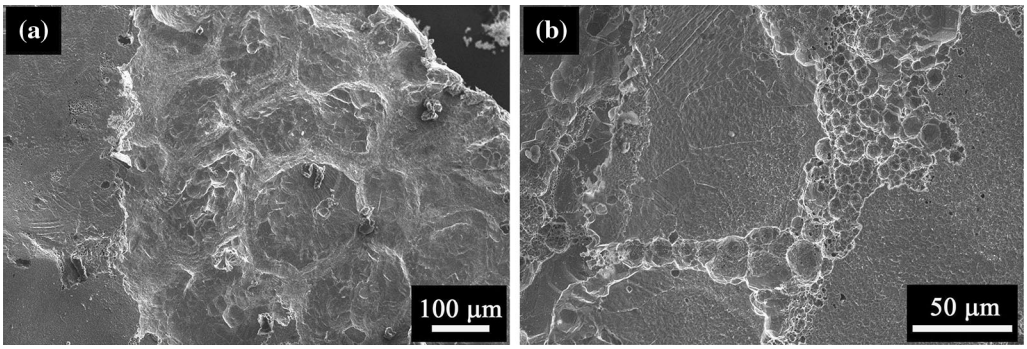

Fig. 7—SEM micrographs of two different regions (*a* and *b*) after dynamic polarization test up to 1 V in 3.5 pct NaCl solution for the harmonic structured stainless steel. (b) is the magnified image from the corroded part of (a) showing the preferential attack in the fine grained regions.

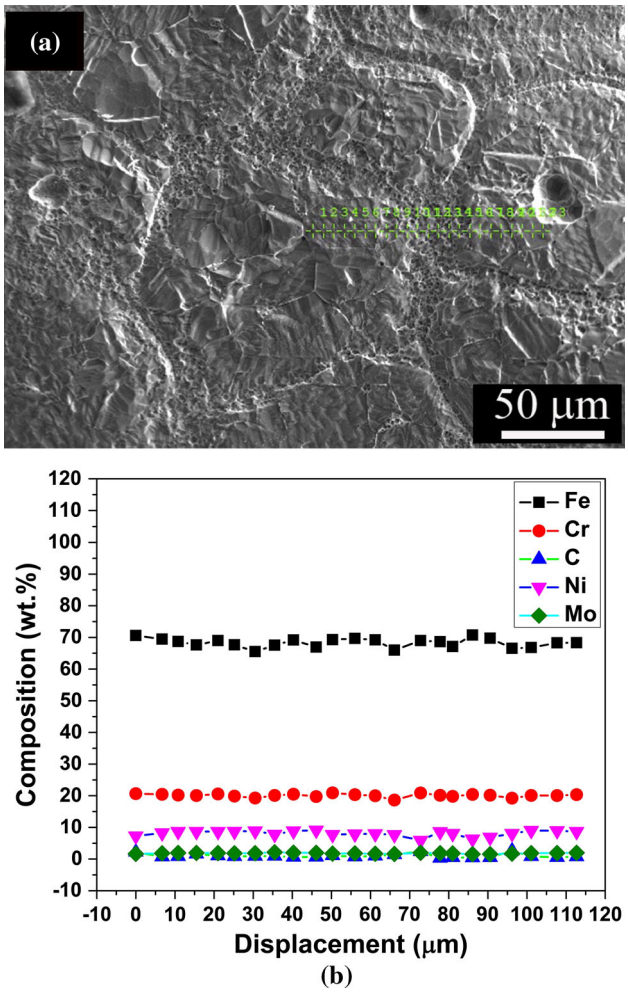

Fig. 8—EPMA analysis of the harmonic steel: (*a*) micrograph showing the line along which compositions have been measured and (*b*) plot showing the quantities of Fe, Cr, Ni, Mn, and C.

In order to compare the pitting behavior of the preceding three stainless steels, cyclic polarization tests were performed, and the corresponding plots are shown in Figure 9. It is clear from Figure 9 that cyclic polarization plots of the nonharmonic and the conventional 304 stainless steel show a larger positive hysteresis loop as compared to that of the harmonic structured

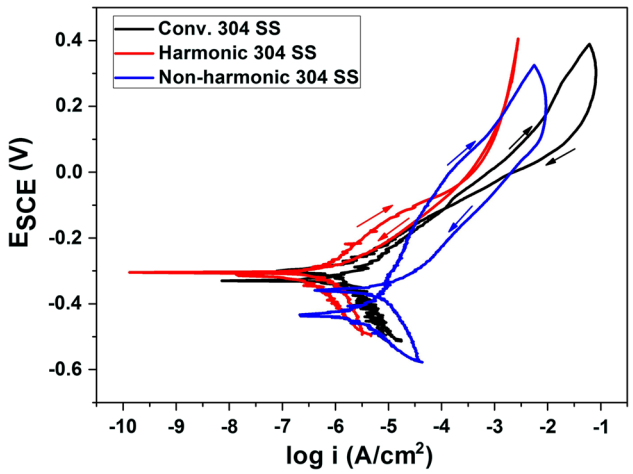

Fig. 9—Cyclic polarization plots of the harmonic, the nonharmonic, and the conventional stainless steels in 3.5 pct NaCl solution.

stainless steel. Contrary to this, the harmonic stainless steel shows a negative hysteresis loop in a smaller potential range, which means that the harmonic steel has some tendency to repair the breakdown at localized areas during reversal of potential. Moreover, the repassivation potentials (E_{rp}) for the harmonic, conventional, and nonharmonic steels are –0.03, –0.1, and –0.35 V, respectively. This also suggests that the pitting tendency is maximum for the nonharmonic steel and that the harmonic steel has the highest pitting resistance. The conventional steel falls in-between. This can be attributed to the fine grains present in the harmonic stainless steel resulting in the formation of extremely fine pits in the harmonic steel (shown by arrowhead) compared to the larger pits formed in the nonharmonic and conventional 304 steels, as shown in the SEM micrographs (Figures 10(a) through (c)) of the specimens after the cyclic polarization tests. Figures 10(a) through (c) also indicate that pitting is most significant in the nonharmonic structured case (Figure 10(c)) as compared to the harmonic structured and conventional stainless steel samples. This is also quite possible, since once the breakdown in the passive layer happens, corrosion proceeds along the broken sites, forming deep pits. Whereas, in the case of the fine-grained section, the

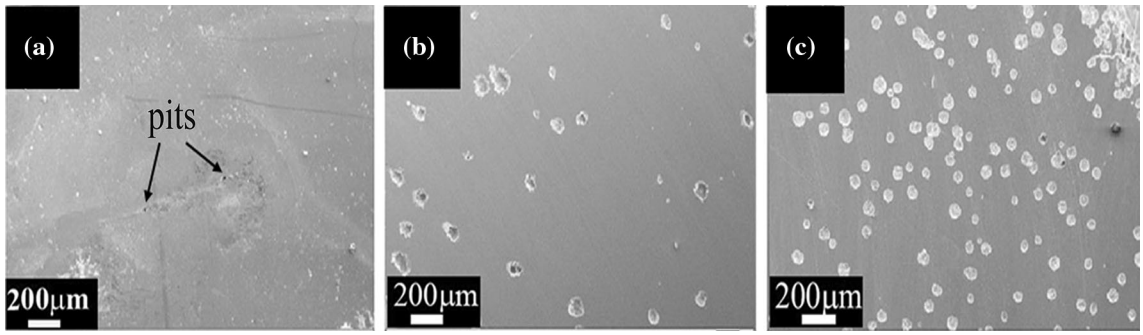

Fig. 10—SEM micrographs after the cyclic polarization test in 3.5 pct NaCl solution for (*a*) the harmonic, (*b*) the conventional, and (*c*) the non-harmonic stainless steel.

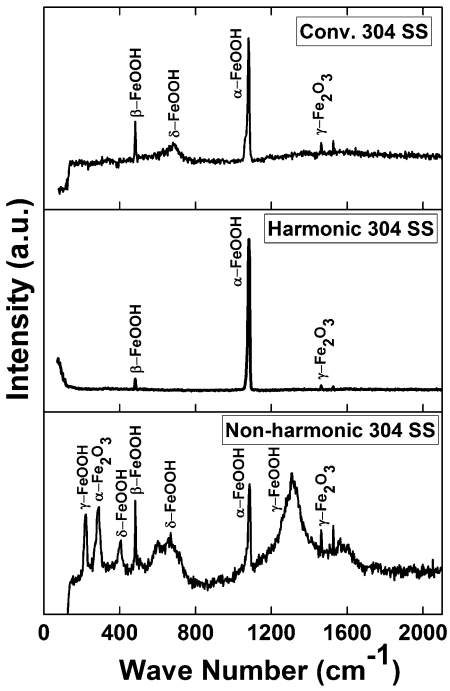

Fig. 11—Raman spectroscopy plots after the dynamic polarization test in 3.5 pct NaCl.

pitting is not severe, since there is continuous formation and destruction of the passive layer along the fine-grained sections and the corrosion mode is of a more uniform type.

Raman spectroscopy analysis of the corroded surface of the specimens after a dynamic polarization test is shown in Figure 11, which shows the constituents of the corrosion product. It was reported in the literature that the increment in the ratio of α-FeOOH and gamma* (total mass of gamma-FeOOH, beta-FeOOH, and magnetite) in the corrosion products leads to a decrease in corrosion rate.[38,39] Raman peaks (Figure 11) were identified and the fraction of α-FeOOH is determined by comparing the area of Raman peaks found to be ~83, ~18, and ~41 pct for the harmonic, nonharmonic, and conventional 304 stainless steels, respectively.[40,41] Therefore, α-FeOOH is the major phase of the corrosion products present on the surface, and the fraction of α-FeOOH was found to be greater in the harmonic structured steel compared to the other two steels. Hence, it can be concluded that the higher fraction of protective α-FeOOH in the harmonic structured steel caused a reduction in the corrosion rate. Interestingly, the conventional steel has an intermediate value of the fraction of α-FeOOH, which can be attributed to its intermediate corrosion rate and other polarization parameters (E_{corr} and R_p). Moreover, the pitting corrosion resistance of the conventional steel is also in-between the harmonic and the nonharmonic steels.

The specimens of the harmonic and nonharmonic steels were cleaned by Clarke's solution (1000 mL hydrochloric acid + 20 g antimony trioxide + 50 g stannous chloride) after exposure to a salt fog environment for 30 days, and the mass loss was determined.[42] The corrosion rates were found to be 0.13 and 0.17 mm/year for the harmonic and nonharmonic structured SUS304L steels, respectively, as measured according to ASTM G1-03.[42] Though the difference in the corrosion rates of both steels is not large, the pitting is severe in the case of the nonharmonic steel sample after the salt fog test (Figure 12(a)) as compared to the harmonic structured steel sample (Figure 12(b)). This finding also suggests that the pitting corrosion resistance of the harmonic structured steel is higher than that of the nonharmonic one, which is in good agreement with the results of the cyclic polarization tests. It should be mentioned that the difference in the corrosion rates in the polarization tests (Table II) and salt spray tests is due to the different natures of the tests. In the salt spray test, the corrosion process is more aggressive due to the alternate drying and wetting cycle. Moreover, the character of the corrosion product changes over the 30 days of the test cycle. On the other hand, the polarization tests are short time tests. Hence, the dynamic change of the sample surface over a longer time frame is not considered in the quick polarization tests. However, the trend in the change of corrosion rates of different structured steels is similar, though the magnitude is different.

In order to understand the cause of the higher pitting corrosion resistance of the harmonic structured steel, as observed from the salt-fog test, the corrosion products formed on the surface of the specimen were analyzed. Figures 13(a) and (b) show the SEM micrographs of the

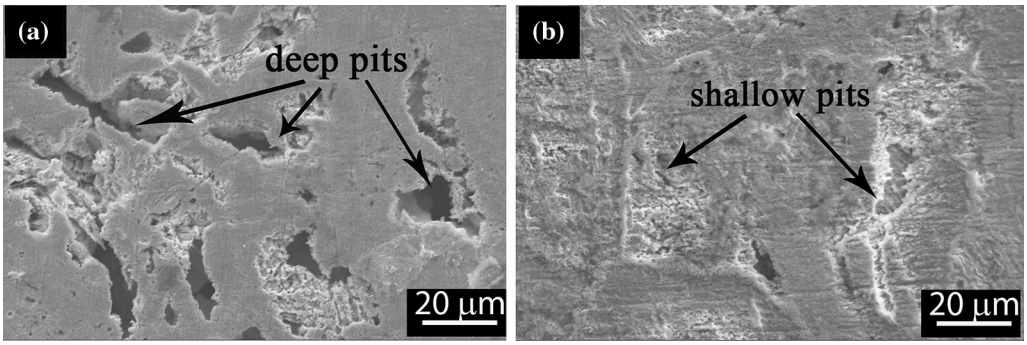

Fig. 12—SEM micrographs of the samples after removal of corrosion products from (*a*) the nonharmonic and (*b*) the harmonic structured stainless steel exposed to salt fog environment for 30 days.

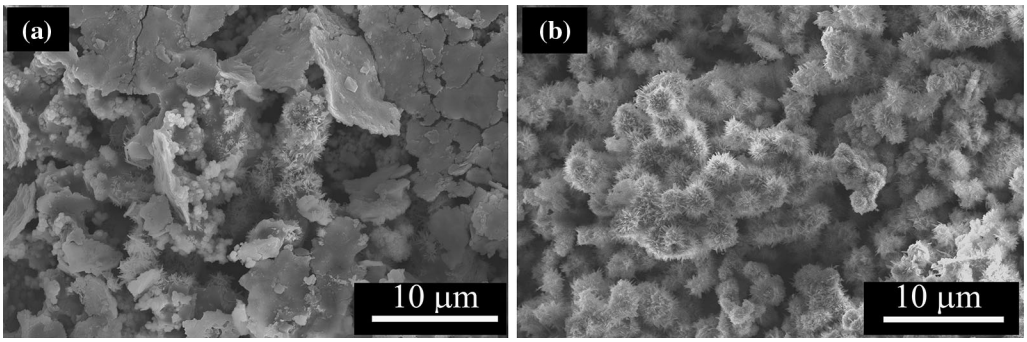

Fig. 13—SEM micrographs of the corrosion product layer showing ''cotton balls'' after exposure to salt fog environment for 30 days of (*a*) the nonharmonic and (*b*) the harmonic structured SUS304L steel.

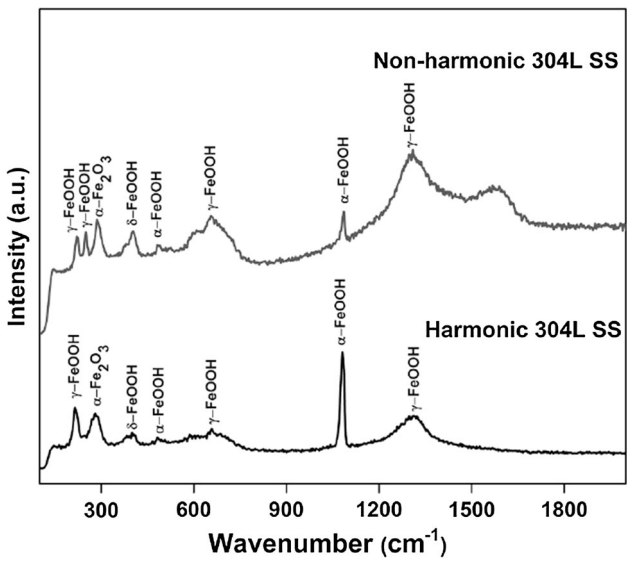

Fig. 14—Raman spectroscopy plots as taken from the corrosion products of the specimens exposed to salt fog environment for 30 days.

corrosion products formed on the specimen of the nonharmonic and harmonic structured steels, respectively, after exposure to a salt fog environment for 30 days. A typical ''cotton ball'' morphology is found in the micrograph of the corrosion products of the harmonic structured SUS304L steel, which was reported to be α-FeOOH, as shown in Figure 13(b).[43,44] The characteristic morphology of α-FeOOH can be seen only in some regions in the case of the nonharmonic structured steel, as shown in Figure 13(a). This is also confirmed by Raman spectroscopy results, as shown in Figure 14. The fractions of α-FeOOH were found to be ~23 and ~11 pct for the harmonic and nonharmonic structured SUS304L steels, respectively. The higher fraction of passive α-FeOOH in the corrosion products formed on the harmonic structured steel, as compared to that of the nonharmonic structured steel, can be attributed as the cause of the increase in the pitting corrosion resistance of the harmonic structured steel.

IV. CONCLUSIONS

It was observed that the SUS304L stainless steel with harmonic structured design shows better corrosion resistance in 3.5 pct NaCl solution as compared to the nonharmonic structured and the conventional 304 stainless steel. Uniform distribution of the fine- and coarse-grained regions, as well as higher grain boundary fractions in the harmonic steel, along with extremely low porosity attribute to its highest corrosion resistance. The shell region of the harmonic structured steel has been found to be more corroded compared to the core. It has been seen that there is no compositional variation in the

shell and core regions in the harmonic structured steel; therefore, chemical change could not be the cause of higher corrosion of the shell region. The large number of grain boundaries present in the shell region was attributed to the high rate of corrosion in this region. The reason for reduction in corrosion resistance of the nonharmonic structured steel was attributed to the presence of significant porosity. Pre-existing pores in the material led to aggravation of the pitting corrosion. The large fraction of passive α-FeOOH present in the harmonic structured steel is also one of the reasons for higher corrosion resistance in that steel.

REFERENCES

1. G.E. Dieter: in *Mechanical Metallurgy*, S.I. Metric, ed., McGraw-Hill Book Company, Singapore, 1988.
2. C.C. Koch: *Mater. Sci. Forum*, 1992, vol. 88, pp. 243–62.
3. B.S. Murty and S. Ranganathan: *Int. Mater. Rev.*, 1998, vol. 43, pp. 101–41.
4. Y. Zhao, X. Liao, Z. Jin, R. Valiev, and Y. Zhu: *Acta Mater.*, 2004, vol. 52, pp. 4589–99.
5. V. Stolyarov, Y. Zhu, I. Alexandrov, T. Lowe, and R. Valiev: *Mater. Sci. Eng. A*, 2001, vol. 299, pp. 59–67.
6. T. Roland, D. Retraint, K. Lu, and J. Lu: *Mater. Sci. Eng. A*, 2007, vols. 445–46, pp. 281–88.
7. P.K. Rai, V. Pandey, K. Chattopadhyay, L.K. Singhal, and V. Singh: *J. Mater. Eng. Perform.*, 2014, vol. 23, pp. 4055–64.
8. K. Lu, J.T. Wang, and W.D. Wei: *J. Appl. Phys.*, 1991, vol. 69, pp. 522–24.
9. U. Erb, A.M. El-Sherik, G. Palumbo, and K.T. Aust: *Nanostruct. Mater.*, 1993, vol. 2, pp. 383–90.
10. Y. Wang, M. Chen, F. Zhou, and E. Ma: *Nature*, 2002, vol. 419, pp. 912–14.
11. C.C. Koch: *Scr. Mater.*, 2003, vol. 49, pp. 657–62.
12. Z. Lee, D.B. Witkin, V. Radmilovic, E.J. Lavernia, and S.R. Nutt: *Mater. Sci. Eng. A*, 2005, vols. 410–411, pp. 462–67.
13. B. Srinivasarao, K. Oh-ishi, T. Ohkubo, T. Mukai, and K. Hono: *Scr. Mater.*, 2008, vol. 58, pp. 759–62.
14. Q.H. Bui: *J. Mater. Sci.*, 2012, vol. 47, pp. 1902–09.
15. D. Orlov, H. Fujiwara, and K. Ameyama: *Mater. Trans. (JIM)*, 2013, vol. 54, pp. 1549–53.
16. C. Sawangrat, O. Yamaguchi, S.K. Vajpai, and K. Ameyama: *Mater. Trans. (JIM)*, 2014, vol. 55, pp. 99–105.
17. S.K. Vajpai, K. Ameyama, M. Ota, T. Watanabe, R. Maeda, T. Sekiguchi, G. Dirass, and D. Tingaud: *IOP Conf. Ser.: Mater. Sci. Eng.*, 2014, vol. 63, p. 012030.
18. Z. Zhang, D. Orlov, S.K. Vajpai, B. Tong, and K. Ameyama: *Adv. Eng. Mater.*, 2015, vol. 17, pp. 791–95.
19. C. Sawangrat, S. Kato, D. Orlov, and K. Ameyama: *J. Mater. Sci.*, 2014, vol. 49, pp. 6579–85.
20. O.P. Ciuca, M. Ota, S. Deng, and K. Ameyama: *Mater. Trans. (JIM)*, 2013, vol. 54, pp. 1629–33.
21. M. Ota, K. Shimojo, S. Okada, S.K. Vajpai, and K. Ameyama: *J. Powder Metall. Min.*, 2014, vol. 3, p. 122.
22. B.V. Mahesh and R.K. Singh: Raman*Metall. Mater. Trans. A*, 2014, vol. 45, pp. 5799–5822.
23. K.D. Ralston and N. Birbilis: *Corrosion*, 2010, vol. 66, pp. 075005–5013.
24. K.D. Ralston, D. Fabijanic, and N. Birbilis: *Electrochim. Acta*, 2011, vol. 56, pp. 1729–36.
25. W. Zeiger, M. Schneider, D. Scharnweber, and H. Worch: *Nanostruct. Mater.*, 1995, vol. 6, pp. 1013–16.
26. W. Ye, Y. Li, and F. Wang: *Electrochim. Acta*, 2006, vol. 51, pp. 4426–32.
27. R.K. Gupta, R.K. Singh Raman, C.C. Koch, and B.S. Murty: *Int. J. Electrochem. Sci.*, 2013, vol. 8, pp. 6791–6806.
28. R. Rofagha, R. Langer, A.M. El-Sherik, U. Erb, G. Palumbo, and K.T. Aust: *Scr. Metall. Mater.*, 1991, vol. 25, pp. 2867–72.
29. E.E. Oguzie, Y. Li, and F.H. Wang: *Electrochim. Acta*, 2007, vol. 52, pp. 6988–96.
30. E. Kus, S. Nutt, and F. Mansfeld: *ECS Trans.*, 2006, vol. 1 (4), pp. 29–42.
31. S. Gollapudi: *Corros. Sci.*, 2012, vol. 62, pp. 90–94.
32. A.M. Xavior and M. Adithan: *J. Mater. Process. Technol.*, 2009, vol. 209, pp. 900–09.
33. Z. Zhang, S.K. Vajpai, D. Orlov, and K. Ameyama: *Mater. Sci. Eng. A*, 2014, vol. 598, pp. 106–13.
34. T. Sekiguchi, K. Ono, H. Fujiwara, and K. Ameyama: *Mater. Trans. (JIM)*, 2010, vol. 51, pp. 39–45.
35. H. Fujiwara, T. Kawabata, H. Miyamoto, and K. Ameyama: *Mater. Trans. (JIM)*, 2013, vol. 54, pp. 1619–23.
36. ASTM B117-11: Standard Practice for Operating Salt Spray (Fog) Apparatus, 2011.
37. ASTM G102-89: Standard Practice for Calculation of Corrosion Rates and Related Information from Electrochemical Measurements, *Annual Book of ASTM Standards* (ASTM, West Conshohocken, PA, 1999) vol. 3, p. 416.
38. T. Kamimura, S. Hara, H. Miyuki, M. Yamashita, and H. Uchida: *Corros. Sci.*, 2006, vol. 48, pp. 2799–2812.
39. M. Yamashita, H. Miyuki, Y. Matsuda, H. Nagano, and T. Misawa: *Corros. Sci.*, 1994, vol. 36, pp. 283–99.
40. Y. Waseda and S. Suzuki: *Characterization of Corrosion Products on Steel Surfaces, Series: Advances in Materials Research,* Springer, New York, NY, 2006, vol. 7.
41. S.J. Oh, D.C. Cook, and H.E. Townsend: *Hyperfine Interact.*, 1998, vol. 112, pp. 59–65.
42. ASTM G1-03: Standard Practice for Preparing, Cleaning, and Evaluating Corrosion Test Specimens, 2011.
43. A. Raman, S. Nasrazadani, and L. Sharma: *Metallography*, 1989, vol. 22, pp. 79–96.
44. R.A. Antunes, I. Costa, and D.L.A de Faria: *Mater. Res.*, 2003, vol. 6, pp. 403–08.